nature COMMUNICATIONS

ARTICLE

DOI: 10.1038/s41467-017-02631-9 OPEN

Reconfiguring crystal and electronic structures of MoS_2 by substitutional doping

Joonki Suh[1,11], Teck Leong Tan[2], Weijie Zhao[3], Joonsuk Park[4], Der-Yuh Lin[5], Tae-Eon Park[6], Jonghwan Kim[7,12], Chenhao Jin[7], Nihit Saigal[8], Sandip Ghosh[8], Zicong Marvin Wong[2,9], Yabin Chen[1], Feng Wang[7,10], Wladyslaw Walukiewicz[1,10], Goki Eda[3] & Junqiao Wu[1,10]

Doping of traditional semiconductors has enabled technological applications in modern electronics by tailoring their chemical, optical and electronic properties. However, substitutional doping in two-dimensional semiconductors is at a comparatively early stage, and the resultant effects are less explored. In this work, we report unusual effects of degenerate doping with Nb on structural, electronic and optical characteristics of MoS_2 crystals. The doping readily induces a structural transformation from naturally occurring 2H stacking to 3R stacking. Electronically, a strong interaction of the Nb impurity states with the host valence bands drastically and nonlinearly modifies the electronic band structure with the valence band maximum of multilayer MoS_2 at the Γ point pushed upward by hybridization with the Nb states. When thinned down to monolayers, in stark contrast, such significant nonlinear effect vanishes, instead resulting in strong and broadband photoluminescence via the formation of exciton complexes tightly bound to neutral acceptors.

[1] Department of Materials Science and Engineering, University of California, Berkeley, CA 94720, USA. [2] Institute of High Performance Computing, Agency for Science, Technology and Research, Singapore 138632, Singapore. [3] Department of Physics, National University of Singapore, 2 Science Drive 3, Singapore 117551, Singapore. [4] Department of Materials Science and Engineering, Stanford University, Stanford, CA 94305, USA. [5] Department of Electronics Engineering, National Changhua University of Education, Changhua 50007, Taiwan. [6] Center for Spintronics, Korea Institute of Science and Technology, Seoul 02792, Korea. [7] Department of Physics, University of California, Berkeley, CA 94720, USA. [8] Department of Condensed Matter Physics and Materials Science, Tata Institute of Fundamental Research, Mumbai 400005, India. [9] Department of Chemistry, National University of Singapore, 3 Science Drive 3, Singapore 117543, Singapore. [10] Materials Sciences Division, Lawrence Berkeley National Laboratory, Berkeley, CA 94720, USA. [11] Present address: Department of Chemistry, University of Chicago, Chicago, IL 60637, USA. [12] Present address: Department of Materials Science and Engineering, Pohang University of Science and Technology, Pohang 790-784, Korea. Correspondence and requests for materials should be addressed to J.S. (email: joonki@uchicago.edu) or to J.W. (email: wuj@berkeley.edu)

Substitutional doping of bulk semiconductors, the atomistic substitution with non-isoelectronic impurities, allows to define the type of majority charge carriers and modulate their concentrations to a wide extent, such that they can electrically functionalize as the key component in electronic and optoelectronic devices. For the emerging two-dimensional (2D) or layered semiconductors such as transition metal dichalcogenides, MX_2 (M = transition metal and X = chalcogen), substitutional doping is highly desired to overcome their natively unipolar conduction[1] and substantial contact resistance[2], despite recent efforts based on surface molecular doping[3,4] and phase transition[5,6]. In this context, substitutional doping in MX_2 has been recently experimentally realized, mainly by replacing the host cation M with other transition metal elements[7–9], often leading to degenerate doping levels of free carriers or even switch in conduction type that was hardly achieved by the other doping techniques[3]. Also, recent theoretical studies report doping-induced modifications in magnetic[10,11] and catalytic[12] properties of MX_2.

The atomic *d*-orbitals in transition metal dopants can exhibit different extents of localization[13]. Namely, they are originally spatially localized with a constant energy level relative to the vacuum level, but these discrete levels may interact with each other to gain dispersion as their wavefunctions overlap, particularly at high doping concentrations. It ultimately results in spatial delocalization of the wavefunctions. Consequently, impurity-related sub-bands may emerge near the band edge of the host, and at high densities they may eventually hybridize with the host bands, causing bandgap modification and redistribution of the density of states (DOS)[14,15]. As expected from the nearly linear, virtual crystal approximation widely adopted for semiconductor alloys[16], however, such band restructuring effects often require considerable concentrations of dopants exceeding a few atomic percent to reach the alloying level, with exceptions identified in the so-called highly mismatched alloys[15]. Such dopants-induced band restructuring effects are believed to become stronger at reduced dimensionalities. Heavy doping may also lead to exotic behavior in reduced dimensionalities. For instance, quantum-confined Urbach tail[17] and dynamic surface exciton quenching[18] were observed in heavily doped zero-dimensional (0D) nanocrystals and one-dimensional (1D) carbon nanotubes, respectively. Yet, delocalization of dopant wavefunction and the resultant band restructuring in 2D semiconductors are still experimentally unresolved thus far, despite the fact that quite unique electronic and optical characteristics[19–21] were observed in heavily doped 2D materials.

Among the suggested cation dopants substituting molybdenum (Mo) in molybdenum disulfide (MoS_2), niobium (Nb) has one less *d*-electron, and is of particular importance from the thermodynamics point of view: it is predicted to have a negative formation energy[22]. In addition, Nb doping in MoS_2 was suggested to induce considerable degree of charge delocalization as studied in electron paramagnetic resonance experiments[23] and first-principles calculations[22], as opposed to the case of native point defects (e.g., sulfur vacancies) which only induce localized and nondispersive (flat-energy level) states deep inside the bandgap[24].

In this work, we report modifications in both crystal structure and electronic structure caused by Nb dopants in monolayer to bulk MoS_2. We show doping-induced structural conversion from 2H to 3R stacking in the layered structure, accompanied by a renormalization of the valence band structure. In the multilayer or bulk, the wavefunctions of Nb dopants hybridize with the host valence band at the center of the Brillouin zone (Γ_V), thereby dramatically reducing the indirect bandgap. In stark contrast, such electronic restructuring is greatly suppressed in the ultimate 2D limit where Γ_V of MoS_2 natively moves down, separating out the Nb states as isolated impurity states, i.e., ionization energy of the impurity states becomes greater due to intrinsically larger bandgap and reduced screening, eventually causing the formation of impurity bound excitons.

Results

Crystal structure of Nb-doped MoS_2. Both Nb-free and Nb-doped MoS_2 single crystals, $Nb_xMo_{1-x}S_2$ ($x = 0$–0.01), were synthesized using the chemical vapor transport methods (see Methods). For the Nb-doped MoS_2 (MoS_2:Nb), three representative doping concentrations were prepared to reach the degenerate doping: 0.1, 0.5, and 1% (where the % is defined as the atomic percent of Nb with respect to the density of host Mo sites). In our previous study, X-ray absorption and structural analysis have been employed to verify the substitutionality of the Nb doping as well as uniform distribution of dopants with no phase separation[7]. In addition, Hall-effect technique confirms that free hole concentrations are consistent with the synthesis condition (Supplementary Figure 1). The polymorphs of the synthesized bulk crystals were determined by convergent beam electron diffraction (CBED), and typical images are presented in Fig. 1c. With an obvious difference in symmetries between the MoS_2 and MoS_2:Nb, the CBED patterns confirm the 2H and 3R stacking for the Nb-free and Nb-doped MoS_2, respectively. The 2H and 3R are two different types of stacking order of MX_2 in the trigonal prismatic coordination, described by the space groups of $P6_3/mmc$ and R3m (Fig. 1a), respectively. Unlike the 2H phase, owing to the non-centrosymmetric crystal symmetry and the resultant pseudo-spin polarization in the valence bands, the 3R phase recently attracts great interests for study of valleytronics[25]. While the 2H phase is found more frequently for semiconducting MX_2, the 3R phase is thermodynamically also stable thanks to the nearly negligible difference between their ground-state total energies, and is observed in most of Nb-doped samples we tested (38 out of 41 crystals; see additional CBED images in Supplementary Figure 2 and Note 1). A triangular shape of screw dislocation spiral is also often observed from the surface of the MoS_2:Nb crystals, confirming their non-centrosymmetric stacking[26] (Supplementary Figure 3). Density functional theory (DFT) calculations were performed to confirm the stacking reconfiguration of MoS_2 from 2H phase in the updoped to 3R phase in the Nb-doped case. In Fig. 1b, the total energy difference between bilayer 2H and 3R MoS_2:Nb (ΔE_0) turns into negative values, −0.13 to −0.41 meV per atom, depending on the Nb doping concentrations. We note that the 3R phase is energetically more stable than the 2H phase once the Nb dopant is added to MoS_2 supercell (the 6×6 (4×4) supercell is employed for Ⓐ and Ⓑ (Ⓒ) doping configurations). And, it becomes increasingly more stable upon further Nb incorporation. In short, it is the thermodynamic driving force that reorders the stacking stability, i.e., the 3R phase will naturally form once the Nb dopants are included in the crystal growth at elevated temperatures of ~1000 °C for > 2 weeks. The relative energetic stability can be related to free-carrier screening by holes residing in the d_{z^2} bands with some delocalization[23] in Nb-doped MoS_2, effectively lowering the total energy of non-centrosymmetric 3R-MoS_2. We note that the 3R phase was also experimentally observed in other heavily doped MoS_2[27]. Furthermore, the dynamic stability of such 3R MoS_2:Nb bilayer is confirmed by the phonon dispersion showing no imaginary part, a criteria employed for other poly types of MoS_2[28,29] (Supplementary Figure 4). Consequently, we conclude that Nb doping provides a reliable route of acquiring the uncommon, non-centrosymmetric structure of MX_2 bulk crystals for potential valleytronic applications, circumventing the need for large-area

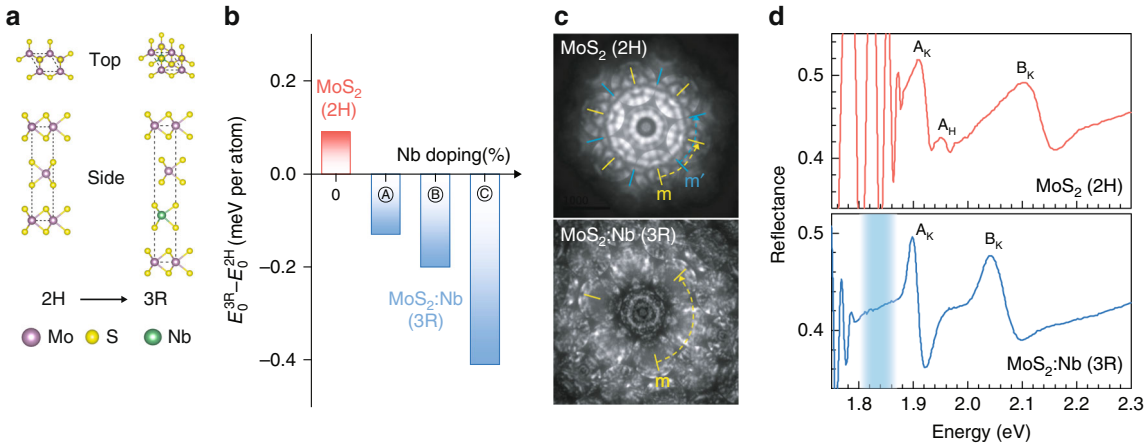

Fig. 1 Crystal structure of undoped and Nb-doped bulk MoS_2. **a** Illustration of modification in stacking order polytypism of MoS_2 by Nb doping (top and side views). The dashed lines show the corresponding single unit cells of 2H and 3R structures. **b** Calculated energy difference of 3R phase with respect to 2H phase, with positive (negative) values indicating that the 2H (3R) phase is more stable. Bilayer MoS_2 system is considered for variable Nb doping concentrations (not to the scale). For the MoS_2:Nb, Ⓐ and Ⓑ are obtained with a 6 × 6 supercell by adding 1 and 2 Nb dopants, respectively. Type Ⓒ is calculated by substituting a Nb dopant into a 4 × 4 supercell. So, their Nb doping concentrations correspond to 1.4, 2.8 and 3.1%, respectively. **c** Convergent beam electron diffraction patterns obtained from the undoped and Nb-doped multilayer MoS_2 at [0001] incidence. Both bulk crystals display mirror symmetries, indicated by yellow and blue lines, for the six-fold (MoS_2, 2H) and three-fold (MoS_2:Nb, 3R), respectively. **d** Optical reflectance spectrum of bulk MoS_2 and MoS_2:Nb taken at 4.5 K. Two main peaks are assigned as A and B exciton transitions at the K point while the additional feature arising from H-point of the Brillouin zone is only observed in undoped MoS_2. The strong absorption below the A exciton in MoS_2:Nb is evidenced by the absence of the Fabry-Perot oscillation which appears in the Nb-free crystal

monolayers, nor delicate adjustment of the growth temperature gradient[25] (the routinely adopted means to stabilize 3R MoS_2).

The rearrangement of stacking order by the substitutional Nb doping also renormalizes the A and B exciton transitions at the K point of the Brillouin zone, as evidenced in optical reflectance spectra for MoS_2 and MoS_2:Nb bulk crystals measured at 4.5 K (Fig. 1d). First, the A exciton feature redshifts slightly by ~10 meV in the MoS_2:Nb crystal, determined by the lineshape fits to a Lorentz oscillator model[30] (Supplementary Figure 5 and Note 2). Second and more notably, the A–B energy splitting decreases from 0.19 to 0.15 eV, i.e., a much greater redshift of the B exciton peak. Also, the flatter dispersion along the K-H path in the 3R system[25] eliminates a distinctive H-point excitonic transition that is normally observable in bulk 2H-MoS_2 at low temperatures[30]. Quantitatively consistent with earlier reports on undoped 3R-MoS_2[25], it can be seen that these renormalization effects in the A and B exciton energies come from the 2H–3R structural transformation in the MoS_2:Nb, rather than a direct electronic effect associated with the Nb doping. Aside from these structural effects, strong and broad absorption is observed at 20–100 meV below the A exciton peak in the MoS_2:Nb crystal (Fig. 1d), and is attributed to Nb impurity states located above the valence band edge at the K point (K_V). Yet, as for what we confirm at the K point, the direct electronic influence of these Nb impurity states on the host MoS_2 bands is negligible, akin to the case of conventional bulk semiconductors in the heavy doping regime.

Electronic restructuring of valence bands in the bilayer case. Few-layer structures were obtained by mechanical isolation from the bulk crystals, which enables further visualization of effects of the different stacking sequences. Figure 2a displays high-resolution transmission electron microscopy (HRTEM) images of bilayers (2L) of undoped MoS_2 and MoS_2:Nb. Here the 2H stacking of undoped MoS_2 (top panel) is easily recognized with no atom located at the center of each hexagon. In the MoS_2:Nb bilayer, on the contrary, additional atomic columns appear in the center of each hexagon, with a slight but noticeable intensity difference between nearest neighbor columns. Atomically precise positioning and stack ordering of layers are possible in such 3R-stacking bilayer with the aid of line intensity profile[31] (Supplementary Figure 6). With extensive HRTEM investigation, we confirm that structurally the Nb doping only induces the 3R polytypism in MoS_2, preserving its single crystallinity without causing extended defects and local lattice distortion.

Bulk MoS_2 is an indirect-bandgap semiconductor with negligible photoluminescence (PL), thus prevents access to its electronic bands in light emission spectroscopy. When the MoS_2 crystal is thinned to a few layers, however, noticeable PL emerges with two major features. A main peak at ~1.85 eV is associated with (hot-carrier) transitions across the direct bandgap at the K-valley, whereas a relatively weak PL peak at lower energies (Fig. 2b) arises from transitions across the indirect bandgap involving the Γ_V, which constitutes a combination of Mo $-$ d_{z^2} and S $-$ p_z orbitals. Since these orbitals extend along the z-direction with strong overlap between neighboring layers, the indirect PL peak acts as an indicator of interlayer coupling: the lower the indirect PL peak energy is, the stronger the interlayer coupling[32]. 3R stacking is known to have a slightly shorter interlayer spacing compared to that of 2H, so the indirect PL of 3R bilayers is expected to redshift. However, to separate the structural (2H vs. 3R) effect from electronic (doped vs. undoped) effect in Nb-doped 3R bilayers, it is necessary to also include Nb-free 3R bilayers in the comparison. Indeed, the indirect PL of Nb-free 3R bilayers redshifts slightly by ~30 meV, as shown in Fig. 2b. In contrast, the observed redshift of indirect PL from the Nb-doped 3R bilayers is much greater, up to ~140 meV, and it indeed monotonically redshifts further with Nb fraction (x). These effects suggest additional mechanism of Nb doping beyond the mere 2H–3R structural conversion.

The unusual evolution of indirect optical transition in 2L-MoS_2:Nb is attributed to a valence band modification by the Nb impurity states. As seen in Fig. 3, the impurity level of Nb replacing Mo (denoted as E_I) is theoretically known to be located below the Γ_V in MoS_2 for both bulk and bilayer cases[33], also judged from the reflectance spectra in Fig. 1d, thus crossing and

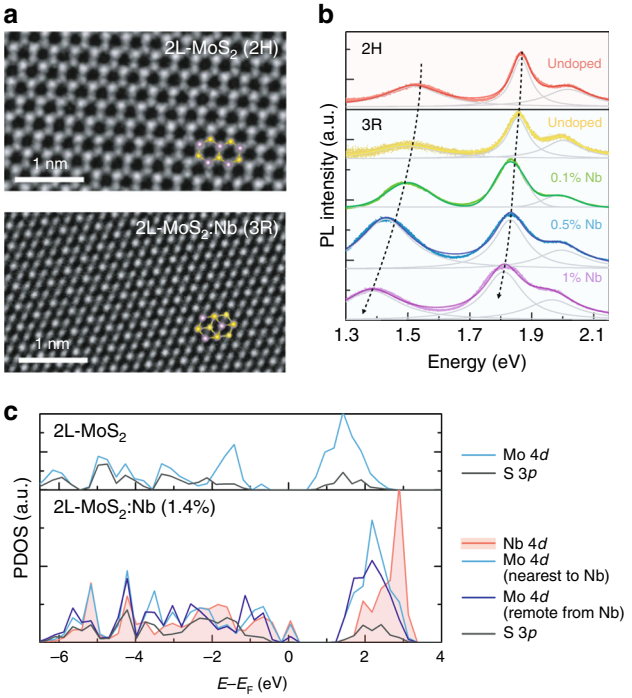

Fig. 2 Beyond the 2H–3R structural transition: Restructuring of valence bands in bilayer Nb-doped MoS_2. **a** High-resolution transmission electron microscopy (HRTEM) images of typical bilayer (2L) MoS_2 and Nb-doped MoS_2 flakes. The insets show a modeled top view of 2H and 3R MoS_2 bilayers with violet and yellow spheres corresponding to Mo and S atoms, respectively, and are superimposed onto the HRTEM images. Here the existence of Nb dopants is not presented due to its substitutionality and indistinguishability from Mo in HRTEM ($Z_{Nb} = 41$ and $Z_{Mo} = 42$). Scale bars, 1 nm. **b** Room temperature photoluminescence (PL) spectra of 2L MoS_2 including both 2H and 3R structures, and MoS_2:Nb with three representative doping concentrations. The arrow line shows the evolution of indirect bandgap to guide the eye. **c** Calculated partial density of states (PDOS) of 2L undoped and Nb-doped MoS_2 (3R-stacked) projected onto the selected atoms, Mo, Nb and S. For the bilayer MoS_2:Nb, one of the 72 Mo atoms is substituted with a Nb dopant atom (corresponding to 1.4% doping) to match the experimental doping level. Also, two representative Mo atoms, the nearest to and remote away from Nb dopants, are shown here to resolve their distinct contributions to the valence band maximum

in resonance with the valence bands. In this case, an upshift of Γ_V (hence a reduction of the indirect bandgap) is expected from a simple two-level repulsion model, as exemplified in similar cases of valence (conduction) bands of GaAs where As is partially substituted with Bi or Sb (N)[14,34]. More generally, this two-level band-anticrossing model has successfully described the electronic band restructuring in a wide range of substitutional semiconductor alloys[15,35,36]. It predicts the restructuring and hybridization of host bands ($E_V(\mathbf{k})$) with impurity states (E_I), giving rise to the two newly formed sub-bands expressed as

$$E_{\pm}(\mathbf{k}) = \begin{vmatrix} E_V(\mathbf{k}) & C\sqrt{x} \\ C\sqrt{x} & E_I \end{vmatrix} \quad (1)$$

where C is a parameter describing the hybridization strength, and x is the fraction of the impurities. For the case of bilayer MoS_2:Nb, $E_V(\mathbf{k})$ and E_I are the original valence band dispersion of MoS_2 and the originally non-dispersive Nb energy level, respectively, and $E_{\pm}(\mathbf{k})$ is the two newly formed sub-bands as a result of the anticrossing interaction between $E_V(\mathbf{k})$ and E_I, as shown in Fig. 3a. Even a sub-1% doping causes a significant band restructuring in MoS_2:Nb, suggesting a strong band-anticrossing interaction with a high interaction parameter, C.

We also performed ab initio calculations on the electronic structures using DFT within the local density approximation and the results confirmed this model. Figure 2c shows the partial density of states (PDOS) plot for 2L undoped and Nb-doped MoS_2 in the 3R-type stacking order. Upon Nb doping, the indirect bandgap becomes narrower and the Fermi level (E_F) downshifts consistent with our experimental observation. As seen from the undoped MoS_2, the band edges of both conduction and valence bands are mainly composed of Mo 4*d* states. For 2L-MoS_2:Nb, the Nb 4*d* state contributes most significantly to the valence band maximum, Γ_V, while its influence on the conduction band minimum is nearly negligible. Notably, contribution from the host Mo 4*d* state to the valence band edge is found to be sensitive to its distance to the Nb dopant; the closer to the Nb atom, the greater contribution of the Mo to the valence band maximum. This is not the case for the conduction band, hence it supports our band-anticrossing-type hybridization between the Nb and Mo 4*d* states at Γ_V, as outlined above. Atomic contribution-resolved band structures further elucidate the case by visualizing the hybridization at Γ_V (Supplementary Figure 7). That is, as the doping concentration increases, the valence band maximum (Γ_V) gains more E_I character from the Nb dopants simply because of the greater fraction of Nb, x; in the meantime, our calculation suggests that the interaction parameter, C, can be simultaneously enhanced due to the closer physical distance to the dopants as x increases, all ultimately driving the indirect PL peak to monotonically redshift with x.

Bound excitons in the monolayer limit. When further thinning down to the monolayer limit, 2H- and 3R-MoS_2 no longer have a structural distinction (Supplementary Figure 8). From the bulk to monolayer, MoS_2 layers transit from indirect to direct bandgap, as well as experience reduced dielectric screening. These effects lead to well-known strong PL and large excitonic binding energy in monolayer MoS_2. For monolayer MoS_2, a drastic self-downshift of the Γ_V point makes the K_V pockets the valence band maximum, across which direct optical transitions take place. In such a system, the Nb impurity states are now located above the valence band maximums, no longer crossing the valence bands of MoS_2 (Fig. 3b) and hence becoming isolated in-gap impurity states. Such reconfiguration of relative location between the host valence bands and the impurity level results in a few notable changes.

First, we observed an enhanced, broad-band and redshifted PL emission at room temperature (RT) from the monolayer MoS_2:Nb, as shown in Fig. 4a. Combined with the corresponding absorption spectra (Supplementary Figure 9 and Note 3), it can be attributed to optically excited excitons (X) binding to neutral acceptor (A^0) resulting in the formation of A^0X complexes. While an ionized acceptor (A^-) does not usually bind an exciton, the binding energy of exciton is in general the highest for a neutral acceptor according to the Haynes rule[37]. As illustrated in Fig. 3, the former (A^-X) and latter (A^0X) cases correspond to the bilayer and monolayer MoS_2:Nb, respectively, under the assumption that E_I becomes a deep impurity level and a portion of acceptors are no longer thermally ionized for the monolayer MoS_2:Nb according to Fermi-Dirac statistics. In this sense, a direct PL of 2L-MoS_2:Nb is only weakly affected by the presence of E_I (Fig. 2b) but that of monolayer MoS_2:Nb substantially changes. It is also noted that such impurity-bound PL becomes even broader and more redshifted upon increase in the Nb doping concentration. Next, PL of the monolayer MoS_2:Nb is seen to be more than an order of magnitude stronger than that of the undoped monolayer

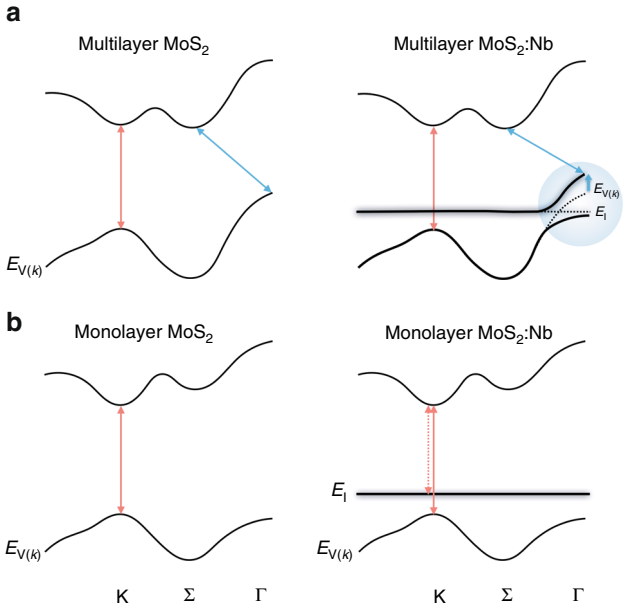

Fig. 3 Band engineering of MoS_2 by Nb doping. Schematic band structures of **a** multilayer, such as bulk and bilayer, and **b** monolayer MoS_2 before (left panel) and after (right panel) degenerate Nb doping. For the case of multilayer MoS_2:Nb, the pristine valence bands of Nb-free MoS_2 are included as dotted black lines for a direct comparison, and the regions in the Brillouin zone (Γ_V) where a significant band restructuring takes place are also highlighted as a blue circle. Direct (impurity-bound) and indirect transitions are indicated by red (dotted) and blue arrow lines, respectively

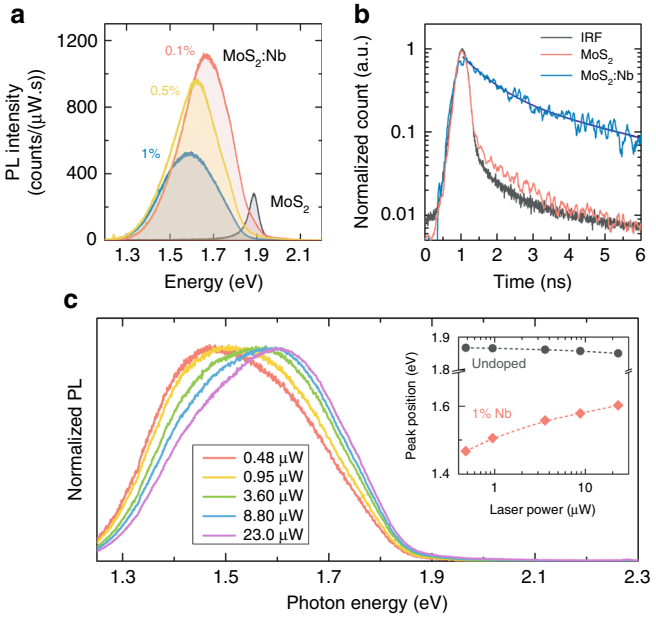

Fig. 4 Photoluminescence in monolayer Nb-doped MoS_2. **a** Room temperature photoluminescence (PL) characteristics of monolayer MoS_2 and MoS_2:Nb. The spectra were collected under excitation with a 4.2 μW Ar-ion laser line (488 nm). **b** Time-resolved PL of monolayer MoS_2 and MoS_2:Nb. Black curve represents the instrumental response function (IRF). **c** A series of PL spectra with different excitation laser power for 1% Nb-doped MoS_2 monolayer. Inset shows the gradual PL peak shift of MoS_2:Nb upon increasing laser input power in comparison with undoped MoS_2 monolayer

MoS_2, with a much elongated PL lifetime as shown in Fig. 4b. That is, while the decay dynamics of the exciton states at ~1.88 eV in undoped MoS_2 is rather fast (lifetime, τ, on the order of 100 ps[38]) approaching the instrumental response function (IRF), the PL at ~1.68 eV in the monolayer MoS_2:Nb shows significantly slower bi-exponential decay dynamics ($\tau_1 = 0.7 \pm 0.05$ ns and $\tau_2 = 4.3 \pm 0.3$ ns). This is in great contrast with the earlier PL studies on native defects like chalcogen atomic vacancies where PL decay times are measured as a few hundred ps[39,40]. Moreover, although such defect-related PL feature is observed only at cryogenic temperatures[24], here the Nb-induced sub-band PL is much brighter and stable even at RT. Doping could indeed, in some cases, enhance radiative efficiency and could, for example, even enable RT lasing in GaAs nanowires[41], yet such remarkable luminescence enhancement has not been reported in 2D semiconductors. Last, PL from undoped and Nb-doped monolayer MoS_2 shows a different laser excitation power dependence (Fig. 4c). As laser power steadily increases, PL in the monolayer MoS_2:Nb, stemming from the impurity-bound excitons as described above, monotonically shifts toward higher energy, as similarly observed for localized excitons[42] whilst the undoped MoS_2 monolayer only displays a slight decrease presumably due to laser heating effect.

Photoluminescence excitation (PLE) spectroscopy was also performed over a wide range of excitation energies to further understand this unusual PL behavior. It can be seen from Fig. 5 that the PLE signal appears when the excitation energy is above the A exciton absorption, and reaches a maximum when the excitation energy is equal to the B exciton absorption, as similarly reported in undoped monolayer MoS_2[43]. However, this enhancement of emission is not observed for excitation at C resonance indicating that an exciton first needs to form to bind to the impurities. Again, this PLE behavior is different from what is known for defect-related emission[44]. The fact that the PLE emission starts only after the excitation energy is higher than the A exciton energy (rather than when the excitation energy is equal to the Nb impurity energy level), is also an indication that the Nb impurity states no longer form a dispersive band in this case (unlike at the Γ_V band in multilayer or bulk). Therefore, the Nb states stay as non-dispersive energy levels not hybridizing with the K_V host bands (Fig. 3b), instead contributing to the formation of bound excitons. Indeed, hybridization of impurity states with the host bands is expected to be much weaker at the Brillouin zone edge (K) than at the center (Γ). This is because the interaction strength (C) in the band anticrossing model becomes the maximum at $\mathbf{k} = 0$ (i.e., at Γ_V), with a rapidly decreasing $\mathbf{k}$-dependence that follows the Fourier transform of the spatially-decaying overlap integral between the impurity wavefunction and the Wannier function of the host bands[45]. Moreover, the hybridization at K_V is further weakened due to the farther energy separation of E_I from $E_V(\mathbf{k})$ at K_V in the monolayer (than Γ_V in multilayer/bulk).

Discussion

We have demonstrated restructuring of layer stacking and electronic bands of MoS_2 by introducing substitutional Nb dopants. It drives the stacking sequence from ABABAB (2H) to ABCABC (3R), resulting in broken inversion symmetry even for multilayer MoS_2. Our study reveals that the Nb impurity states in the bulk are quite dispersive and strongly interact with the extended states of host valence band, which is also supported by theoretical analysis. Strong interaction mainly occurs at the Γ_V of the Brillouin zone for multilayer or bulk MoS_2, suggesting a valence band hybridization. It is highlighted that all the structural and electronic modifications in multilayer MoS_2:Nb happen still within the relatively low substitutional fractions of doping (rather than

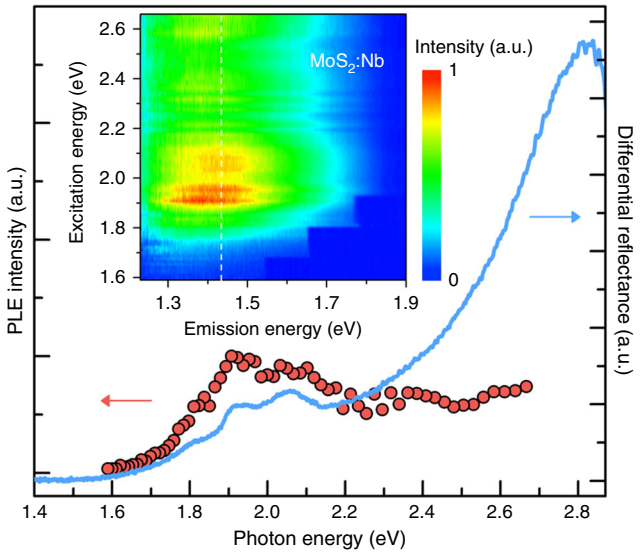

Fig. 5 Photoluminescence excitation (PLE) data of the monolayer MoS_2:Nb (1%). Left and right *y* axis correspond to PL emission energy at 1.43 eV and differential reflectance spectra ($\Delta R/R$), respectively, as a function of excitation energy. Top inset displays PLE intensity 2D map where the color scale represents emission intensity, and was collected with an excitation power of ~0.5 μW at 300 K

alloying). In contrast, in the case of monolayer, the Nb dopants acting as non-interacting impurity states significantly affect the excitonic transition along the K valley. Monolayer of MoS_2:Nb shows a distinctly strong, redshifted and long-lifetime PL monotonically depending on Nb doping concentrations. Our investigation is a step forward towards the possibility of enhancing optoelectronic performance and tuning excitonic effects in 2D semiconductors for potential applications in solid-state devices.

Methods

Materials preparation. Undoped and Nb-doped MoS_2 single crystals were grown by a chemical vapor transport (CVT) method with the use of I_2 as a transport agent. For comparison, natural 2H-MoS_2 crystals were also purchased from SPI Supplies. High purity elements including Mo, S, Nb (all 99.99% purity), and the iodine transport agent were used for the crystal growth. The molar ratio of Mo/S was kept to 1:2 and the substitutional doping concentrations of niobium were designed to become 0.1, 0.5% and 1%, respectively. Afterwards, all reactants were placed in quartz tubes that were evacuated below ~2×10^{-5} Torr and sealed by an oxyhydrogen flame. A horizontal three-zone furnace was utilized to maintain an optimal temperature gradient for the diffusion of iodine transport agent. The quartz tubes were placed into the furnace where the high temperature zone was set at 1050 °C and the low temperature zone was set at 935 °C for 720 h.

Structural characterization. Both convergent beam electron diffraction (CBED) patterns and high-resolution transmission electron microscopy (HRTEM) images were acquired on a FEI Titan environmental TEM 80–300 at 80 kV accelerating voltage. A negative spherical aberration imaging technique with monochromated electron beam was used for HRTEM images of bilayer samples.

Optical measurements. The reflectance measurements on the bulk crystals used light from a 75 W Xenon lamp dispersed by a 1/2 m grating monochromator and a photo-multiplier tube detector, with the sample cooled using a continuous flow liquid He cryostat. Time-resolved photoluminescence measurements were performed using the time-correlated single-photon counting technique at room temperature. MoS_2 samples were excited with an ultrafast optical pulse of photon energy of 2.06 eV and power of 4.5 μJ/cm^2. Pulse duration and repetition rate were 50 ps and 20 MHz, respectively. The PL spectra were obtained with Raman spectrometers in the back scattering geometry and continuous wave 488 nm laser as the excitation source. For photoluminescence excitation (PLE) measurements, a Fianium supercontinuum white laser (SC450) coupled to a laser line tuneable filter (LLTF) was used to provide excitation sources. The excitation lasers, ranging from 460 nm to 760 nm, have a bandwidth of 1–2 nm and their power was kept below 0.5 μW for all the measurements in order to keep the excitation rate in the linear regime and to avoid possible damage to the samples. Multiple measurements were made for each sample to check the reproducibility of the results.

Electronic structure calculations. Density functional theory (DFT) calculations were performed on the bilayer MoS_2 structures to elucidate their bandstructures before and after Nb doping. Geometry optimizations were performed using DFT implemented in the Vienna Ab initio Simulation Package (VASP)[46,47] within a Projected Augmented Wave (PAW)[48] basis and with the Perdew, Burke and Ernzerhof (PBE) functional[49], ensuring sufficient vacuum (at least 20 Å) between periodic images along the *z*-direction (perpendicular to the MoS_2 plane) to minimize spurious interactions. During structural optimization, all atomic coordinates and lattice vectors were fully relaxed until the absolute value of the forces acting on each atom was less than 0.01 eV/Å. We checked that sufficient vacuum remains after relaxation. Plane-wave cutoffs were set to 400 eV and van der Waals interactions were accounted for via the DFT-D2 scheme[50]. For both undoped and Nb-doped MoS_2, a 6×6 supercell was used along with a $4 \times 4 \times 1$ **k**-point grid, unless otherwise stated, with the Monkhorst-Pack sampling[51].

Data availability. The data that support the findings of this study are available from the corresponding authors on request.

Received: 19 May 2017 Accepted: 15 December 2017
Published online: 15 January 2018

References

1. Jariwala, D., Sangwan, V. K., Lauhon, L. J., Marks, T. J. & Hersam, M. C. Emerging device applications for semiconducting two-dimensional transition metal dichalcogenides. *ACS Nano* **8**, 1102–1120 (2014).
2. Allain, A., Kang, J., Banerjee, K. & Kis, A. Electrical contacts to two-dimensional semiconductors. *Nat. Mater.* **14**, 1195–1205 (2015).
3. Behura, S. & Berry, V. Interfacial nondegenerate doping of MoS_2 and other two-dimensional semiconductors. *ACS Nano* **9**, 2227–2230 (2015).
4. Choi, M. S. et al. Lateral MoS_2 p–n junction formed by chemical doping for use in high-performance optoelectronics. *ACS Nano* **8**, 9332–9340 (2014).
5. Saha, D. & Mahapatra, S. Anisotropic transport in 1T' monolayer MoS_2 and its metal interfaces. *Phys. Chem. Chem. Phys.* **19**, 10453–10461 (2017).
6. Kappera, R. et al. Phase-engineered low-resistance contacts for ultrathin MoS_2 transistors. *Nat. Mater.* **13**, 1128–1134 (2014).
7. Suh, J. et al. Doping against the native propensity of MoS_2: degenerate hole doping by cation substitution. *Nano. Lett.* **14**, 6976–6982 (2014).
8. Lin, Y.-C. et al. Properties of individual dopant atoms in single-layer MoS_2: atomic structure, migration, and enhanced reactivity. *Adv. Mater.* **26**, 2857–2861 (2014).
9. Zhang, K. et al. Manganese doping of monolayer MoS_2: the substrate is critical. *Nano Lett.* **15**, 6586–6591 (2015).
10. Zhao, P. et al. Electronic and magnetic properties of Re-doped single-layer MoS_2: a DFT study. *Comput. Mater. Sci.* **128**, 287–293 (2017).
11. Ramasubramaniam, A. & Naveh, D. Mn-doped monolayer MoS_2: an atomically thin dilute magnetic semiconductor. *Phys. Rev. B* **87**, 195201 (2013).
12. Deng, J. et al. Triggering the electrocatalytic hydrogen evolution activity of the inert two-dimensional MoS_2 surface via single-atom metal doping. *Energy Environ. Sci.* **8**, 1594–1601 (2015).
13. Vogl, P. Transition-metal impurities in semiconductors. In *Advances in Solid State Physics* Vol. 25 (ed. Haug, R.) 563–571 (Springer Berlin Heidelberg, Berlin, Heidelberg, 1985).
14. Shan, W. et al. Band anticrossing in GaInNAs alloys. *Phys. Rev. Lett.* **82**, 1221 (1999).
15. Wu, J., Shan, W. & Walukiewicz, W. Band anticrossing in highly mismatched III–V semiconductor alloys. *Semicond. Sci. Technol.* **17**, 860–869 (2002).
16. Jaros, M. Electronic properties of semiconductor alloy systems. *Rep. Prog. Phys.* **48**, 1091–1154 (1985).
17. Mocatta, D. et al. Heavily doped semiconductor nanocrystal quantum dots. *Science* **332**, 77–81 (2011).
18. Crochet, J. J., Duque, J. G., Werner, J. H. & Doorn, S. K. Photoluminescence imaging of electronic-impurity-induced exciton quenching in single-walled carbon nanotubes. *Nat. Nanotechnol.* **7**, 126–132 (2012).
19. Kiriya, D., Tosun, M., Zhao, P., Kang, J. S. & Javey, A. Air-stable surface charge transfer doping of MoS_2 by benzyl viologen. *J. Am. Chem. Soc.* **136**, 7853–7856 (2014).
20. Mouri, S., Miyauchi, Y. & Matsuda, K. Tunable photoluminescence of monolayer MoS_2 via chemical doping. *Nano. Lett.* **13**, 5944–5948 (2013).
21. Sun, Q.-Q. et al. The physics and backward diode behavior of heavily doped single layer MoS_2 based p-n junctions. *Appl. Phys. Lett.* **102**, 093104 (2013).

22. Ivanovskaya, V. et al. Ab initio study of bilateral doping within the MoS_2-NbS_2 system. *Phys. Rev. B* **78**, 134104 (2008).
23. Title, R. S. & Shafer, M. W. Band structure of the layered transition-metal dichalcogenides: an experimental study by electron paramagnetic resonance on Nb-doped MoS_2. *Phys. Rev. Lett.* **28**, 808 (1972).
24. Tongay, S. et al. Defects activated photoluminescence in two-dimensional semiconductors: interplay between bound, charged, and free excitons. *Sci. Rep.* **3**, 2657 (2013).
25. Suzuki, R. et al. Valley-dependent spin polarization in bulk MoS_2 with broken inversion symmetry. *Nat. Nanotechnol.* **9**, 611–617 (2014).
26. Shearer, M. J. et al. Complex and noncentrosymmetric stacking of layered metal dichalcogenide materials created by screw dislocations. *J. Am. Chem. Soc.* **139**, 3496–3504 (2017).
27. Tiong, K. K., Liao, P. C., Ho, C. H. & Huang, Y. S. Growth and characterization of rhenium-doped MoS_2. *J. Cryst. Growth* **205**, 543–547 (1999).
28. Qian, X., Liu, J., Fu, L. & Li, J. Quantum spin Hall effect in two-dimensional transition metal dichalcogenides. *Science* **346**, 1344–1347 (2014).
29. Saha, D. & Mahapatra, S. Atomistic modeling of the metallic-to-semiconducting phase boundaries in monolayer MoS_2. *Appl. Phys. Lett.* **108**, 253106 (2016).
30. Saigal, N. & Ghosh, S. H-point exciton transitions in bulk MoS_2. *Appl. Phys. Lett.* **106**, 182103 (2015).
31. Lu, X. et al. Rapid and nondestructive identification of polytypism and stacking sequences in few-layer molybdenum diselenide by raman spectroscopy. *Adv. Mater.* **27**, 4502–4508 (2015).
32. Splendiani, A. et al. Emerging photoluminescence in monolayer MoS_2. *Nano. Lett.* **10**, 1271–1275 (2010).
33. Chanana, A. & Mahapatra, S. Theoretical insights to niobium-doped monolayer MoS_2-Gold Contact. *IEEE Trans. Electron Devices* **62**, 2346–2351 (2015).
34. Alberi, K. et al. Valence-band anticrossing in mismatched III-V semiconductor alloys. *Phys. Rev. B* **75**, 045203 (2007).
35. Wu, J. et al. Origin of the large band-gap bowing in highly mismatched semiconductor alloys. *Phys. Rev. B* **67**, 035207 (2003).
36. Wu, J. et al. Band anticrossing in $GaP_{1-x}N_x$ alloys. *Phys. Rev. B* **65**, 241303 (2002).
37. Klingshirn, C. F. *Semiconductor Optics*, 4 edn (Springer Berlin Heidelberg: Berlin, Heidelberg, 2012).
38. Amani, M. et al. Near-unity photoluminescence quantum yield in MoS_2. *Science* **350**, 1065–1068 (2015).
39. You, Y. et al. Observation of biexcitons in monolayer WSe_2. *Nat. Phys.* **11**, 477–481 (2015).
40. Lui, C. H. et al. Trion-induced negative photoconductivity in monolayer MoS_2. *Phys. Rev. Lett.* **113**, 166801 (2014).
41. Burgess, T. et al. Doping-enhanced radiative efficiency enables lasing in unpassivated GaAs nanowires. *Nat. Commun.* **7**, 11927 (2016).
42. Gao, X. et al. Investigation of localized states in GaAsSb epilayers grown by molecular beam epitaxy. *Sci. Rep.* **6**, 29112 (2016).
43. Kozawa, D. et al. Photocarrier relaxation pathway in two-dimensional semiconducting transition metal dichalcogenides. *Nat. Commun.* **5**, 4543 (2014).
44. Kumar, R., Verzhbitskiy, I. & Eda, G. Strong optical absorption and photocarrier relaxation in 2-D semiconductors. *IEEE J. Quantum Electron.* **51**, 0600206 (2015).
45. Wu, J., Walukiewicz, W. & Haller, E. E. Band structure of highly mismatched semiconductor alloys: coherent potential approximation. *Phys. Rev. B* **65**, 233210 (2002).
46. Kresse, G. & Furthmüller, J. Efficiency of ab-initio total energy calculations for metals and semiconductors using a plane-wave basis set. *J. Comput. Mater. Sci.* **6**, 15–50 (1996).
47. Kresse, G. & Furthmüller, J. Efficient iterative schemes for ab initio total-energy calculations using a plane-wave basis set. *Phys. Rev. B* **54**, 11169–11186 (1996).
48. Blochl, P. E. Projector augmented-wave method. *Phys. Rev. B* **50**, 17953–17979 (1994).
49. Perdew, J. P., Burke, K. & Ernzerhof, M. Generalized gradient approximation made simple. *Phys. Rev. Lett.* **77**, 3865–3868 (1996).
50. Grimme, S. Semiempirical GGA-type density functional constructed with a long-range dispersion correction. *J. Comput. Chem.* **27**, 1787–1799 (2006).
51. Monkhorst, H. J. & Pack, J. D. Special points for Brillouin-zone integrations. *Phys. Rev. B* **13**, 5188–5192 (1976).

Acknowledgements

This work was supported by the Director, Office of Science, Office of Basic Energy Sciences, Materials Sciences and Engineering Division, of the U.S. Department of Energy under Contract No. DE-AC02-05CH11231. W.W. and Y.C. acknowledge support from the Singapore-Berkeley Research Initiative for Sustainable Energy (SinBeRISE). G.E. acknowledges Singapore National Research Foundation, Prime Minister's Office, Singapore, for funding the research under its Medium-sized Centre program as well as NRF Research Fellowship (NRF-NRFF2011-02). T.L.T. acknowledges the use of high-performance computing facilities in A*STAR Computational Resource Centre (ACRC) in Singapore for the DFT computations performed in this work. D.-Y.L acknowledges the financial support from the Ministry of Science and Technology of Taiwan, Republic of China under contract No. MOST 105-2112-M-018-006. We thank Prof. Sefaattin Tongay and Dr. Can Ataca for helpful discussions in an early stage of the work. Prof. Y. Iwasa and R. Suzuki are also highly appreciated for providing undoped 3R MoS_2 crystals.

Author contributions

J.S. and J.W. conceived and supervised the project. J.S., W.Z., T.-E.P. and G.E. fabricated the samples, conducted the optical and electrical measurements, and analyzed the data. J. K. C.J. and F.W carried out TRPL measurements. N.S. and S.G. helped the reflectance measurements. T.L.T. and Z.M.W. performed the theoretical calculations. D.-Y.L. grew the samples. J.P. performed TEM characterizations. J.S. and J.W. wrote the manuscript. All authors discussed the results and commented on the paper.

Additional information

Supplementary Information accompanies this paper at https://doi.org/10.1038/s41467-017-02631-9.

Competing interests: The authors declare no competing financial interests.

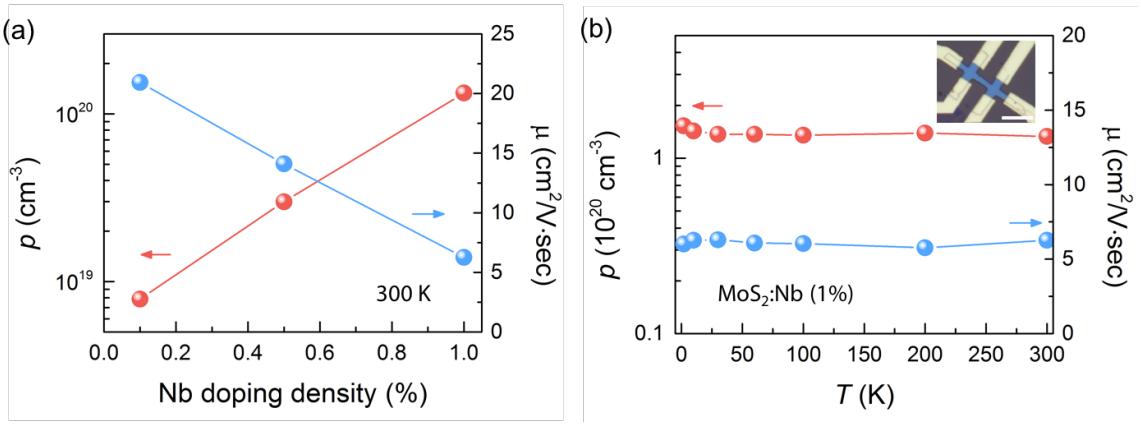

Supplementary Figure 1 | **(a)** Room-temperature hole concentration and mobility as a function of Nb doping density. Hall-effect data for 0.5% Nb doping were taken from Ref #6. **(b)** Temperature dependent carrier concentration and mobility for 1% Nb-doped MoS_2. Inset scale bar, 10 µm.

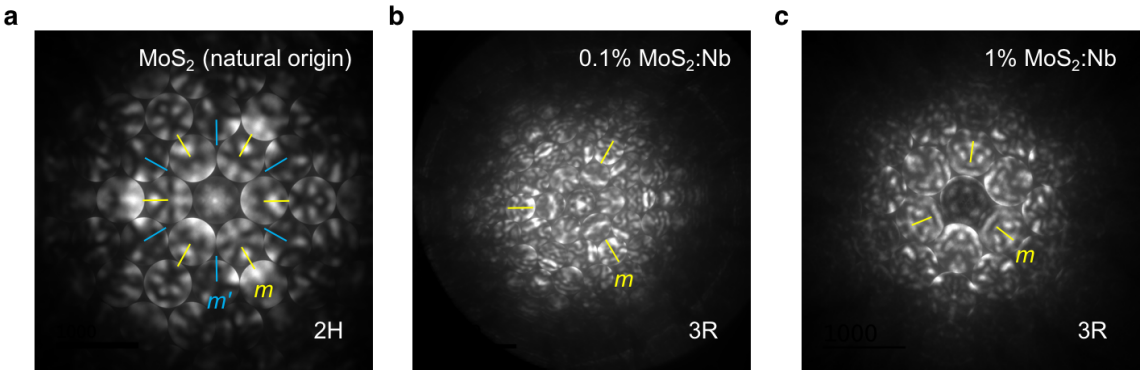

Supplementary Figure 2 | Additional CBED patterns acquired from commercially available MoS_2 (natural origin) (**a**), and 0.1% and 1% Nb-doped MoS_2 crystals (**b,c**).

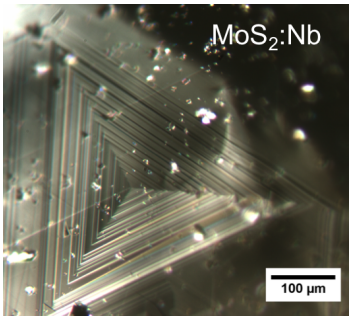

Supplementary Figure 3 | **Optical microscopy image of a screw dislocation spiral.** Optical micrograph taken from the surface of Nb-doped MoS_2 (0.5%) crystal displaying a clear triangular feature as previously observed in undoped 3R-MoS_2[1]. We note, however, that the MoS_2:Nb simultaneously shows the mixed character of triangular and hexagonal spirals, possibly implying that 2H and 3R may co-exist in MoS_2:Nb.

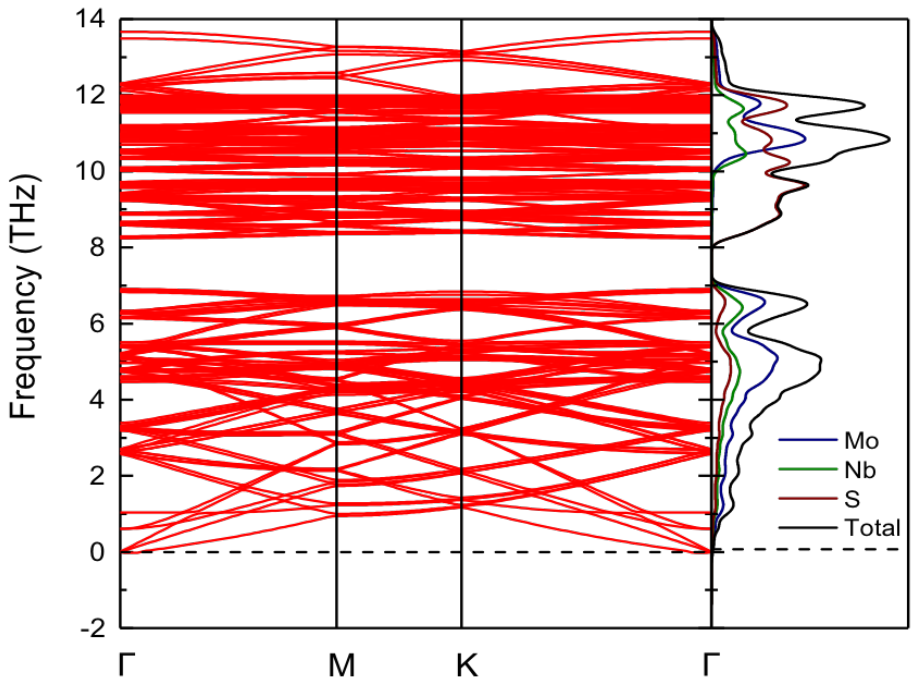

Supplementary Figure 4 | Phonon dispersion and corresponding phonon density of states (DOS) of the Nb-doped 3R-MoS_2 supercell. The phonon calculations of the relaxed Nb-doped MoS_2 4 × 4 supercell were carried out using the PHONOPY code[2], using the finite atomic displacements method with an amplitude of 0.01 Å to obtain the atomic forces within the supercell. This is followed by the dynamical matrix approach to acquire the phonon frequencies.

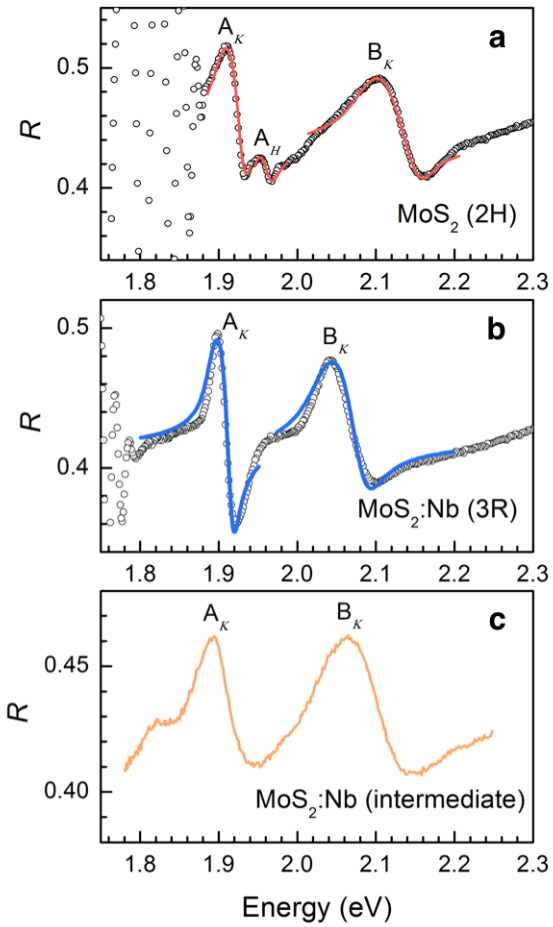

Supplementary Figure 5| Micro-reflectance spectra measured from undoped MoS_2 (**a**) and Nb-doped MoS_2 (**b**) crystals. Distinctive intermediate phase was also observed from some local areas of Nb-doped MoS_2 (**c**). All spectra were taken at 4.5 K.

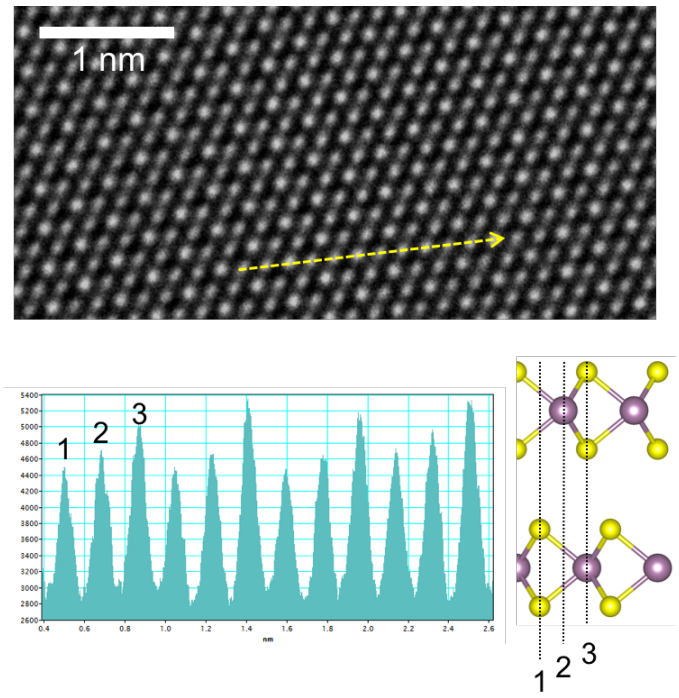

Supplementary Figure 6 | 3R-type bilayer Nb-doped MoS_2. (Top panel) High-resolution transmission electron microscopy image of bilayer Nb-doped MoS_2, clipped from Fig. 2a. (Bottom panels) Corresponding line intensity profile and illustration of atomic model of 3R bilayer. A hexagonal pattern with the measured 1.82 Å lattice spacing is consistent with earlier reports[3,4].

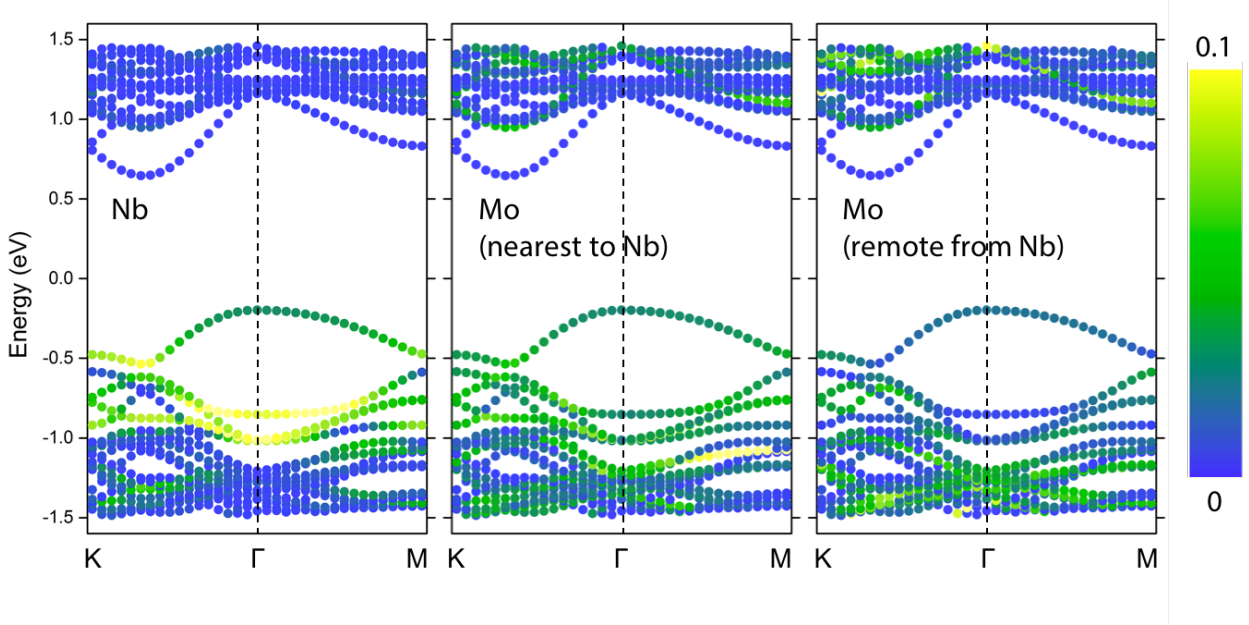

Supplementary Figure 7| Band structures of bilayer 3R Nb-doped MoS_2 projected onto the Nb and Mo atoms. For Mo, the projections are made on two atoms with different distances from Nb dopant for comparison. A 4 × 4 supercell is used, and it is found that $E_F = -0.35$ eV. The color scale indicated the magnitude of the projection.

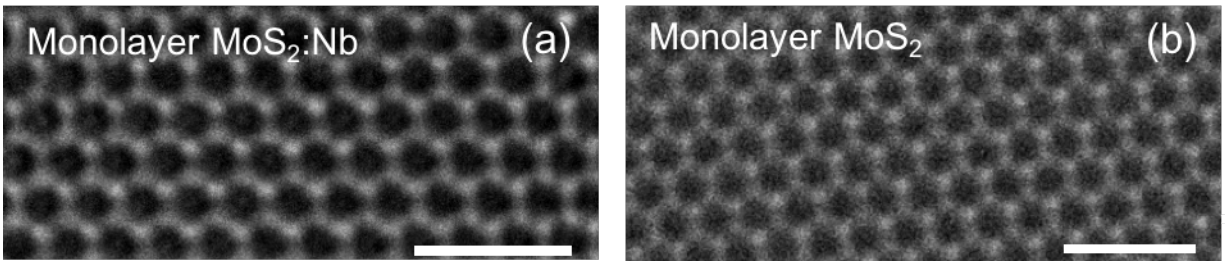

Supplementary Figure 8| Spherical aberration-corrected high-resolution transmission electron microscopy (HRTEM) images with sub-Å resolution acquired from Nb-doped (**a**) and Nb-free (**b**) monolayers, respectively. Both scale bars correspond to 1 nm.

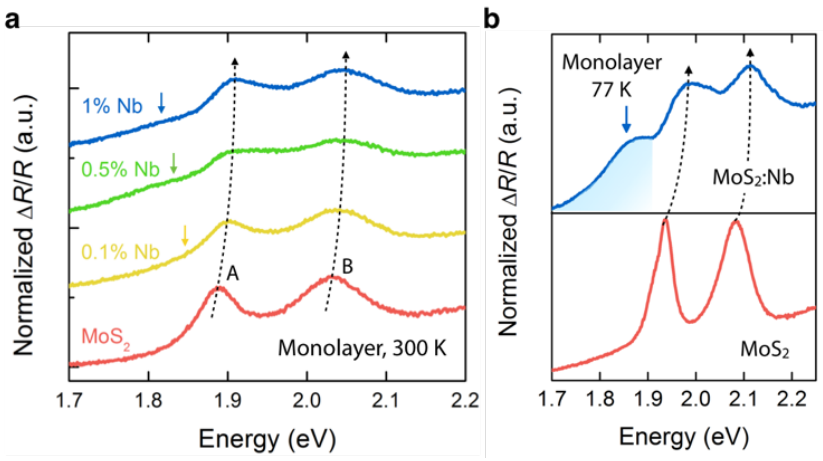

Supplementary Figure 9| Difference reflection spectra ($\Delta R/R$) from monolayer MoS_2 and MoS_2:Nb (**a**) The normalized $\Delta R/R$ for different monolayers measured at 300 K. Corresponding doping levels are indicated, and dotted lines show a blueshift in the A and B exciton levels to guide the eye. (**b**) Representative low-temperature differential reflectivity spectra taken at 77 K from a MoS_2:Nb monolayer with 0.5% of Nb. Blue shade defines the sub-bandgap peak associated with the Nb states.

Supplementary Note 1: Convergent beam electron diffraction

Extensive structural analysis was performed on multiple samples by convergent beam electron diffraction (CBED) in order to determine and distinguish the phase of the synthesized bulk crystals. A total of 51 crystal samples have been investigated. During our investigation, all undoped MoS_2 crystals (9 out of 9) were determined to have 2H stacking ($P6_3/mmc$) regardless of their production origin; chemical vapor transport (top panel in Fig. 1b) and natural resource (SPI supplies, Supplementary Figure 1a). Upon niobium (Nb) doping, the CBED patterns clearly display 3R features with fewer mirror symmetries (R3m). Only a small fraction of Nb-doped MoS_2 flakes (3 out of 42, ~7%) possesses the 2H stacking, and this small fluctuation does not invalidate our conclusion of the stacking restructuring, given the fact that even undoped MoS_2 crystals were reported to consist of ~10% 3R or mixed phase of 2H and 3R[5]. In addition to the representative image (Fig. 1b in a main text) recorded from 0.5% Nb-doped MoS_2 (MoS_2:Nb) crystal, Supplementary Figure 1b and c correspond to 0.1% and 1% doped samples, respectively, confirming the 3R structure of MoS_2:Nb at all degenerate doping levels we employed.

Supplementary Note 2: Low-temperature reflectance spectrum from the surfaces of bulk crystals

Supplementary Figure 3 shows the reflectance spectrum of bulk MoS_2 and Nb-doped MoS_2 (MoS_2:Nb) at 4.5 K. The observed dominant transitions in the spectrum were fit starting with a dielectric function $\varepsilon(E)$ of the form

$$\varepsilon(E) = \varepsilon_b + \frac{C}{E_0^2 - E^2 - i\Gamma E} \quad (1),$$

where ε_b is the background dielectric constant and the rest is the contribution from a particular exciton transition according to the Lorentz oscillator model[6]. Here E is the photon energy while E_0, Γ, and C are the transition energy, homogeneous broadening and amplitude parameter for the transition, respectively. The exciton contribution to $\varepsilon(E)$ was further convolved with a Gaussian to account for the large inhomogeneous broadening[7]. For undoped MoS_2 crystal, the transition energies obtained through fitting using equation (S1) are 1.916, 1.958 and 2.115 eV and 2.143 eV. These can be identified as A_K, A_H, B_K and B_H transitions respectively, of the most common 2H polymorph of MoS_2[6]. The B_K and B_H transitions are unresolved here but can be distinguished in a modulated reflectance measurement[6]. In contrast, most of MoS_2:Nb crystals only show distinct A_K (B_K) of 1.904 (2.056) eV implying its 3R stacking. No separate H-point transition is observed although the A_K still has reasonably narrow width. Additionally, we note that some parts of MoS_2:Nb have a slightly different spectrum as shown in Supplementary Figure 3c. It also displays two main transitions (A_K and B_K), redshifted A_K and no H-point feature like 3R phase. The energy splitting, E_B-E_A, is however larger than that for 3R although it is not as large as that of 2H. Therefore, it can be regarded as the intermediate phase between 2H and 3R of MoS_2, presumably mixed stacking sequences considering their broad features and median nature[5].

Supplementary Note 3: Absorption spectra of undoped and Nb-doped MoS_2 monolayer

Opposite to the redshift in PL spectra, absorption spectra reveals a slight blueshift in the A and B exciton energies in MoS_2:Nb monolayers, as recorded using differential reflectance and shown in Supplementary Figure 5. They also possess a slight dependence on the doping level, and the shift reaches ~20 meV at the highest doping concentration of 1%. In addition to these main excitonic peaks, a long low-energy tail (arrows in Supplementary Figure 5a) was observed for all monolayer MoS_2:Nb samples. Lower temperatures allow clearer detection of the absorption shoulder at ~100 meV below the A exciton resonance, which is in agreement in energy with the impurity-mediated PL peak shown in Figure 4a. In order to understand the slight blueshift of the A and B exciton peaks, we first consider the Burstein-Moss (B-M) shift, as done for other, heavily doped MoS_2 system[8]. The B-M shift is the blueshift in absorption energy across the fundamental bandgap of a degenerately *n* (*p*)-type doped semiconductor because the edge of its conduction (valence) band is no longer completely empty (filled) and hence fully accessible for optical transitions. Quantitatively, using $\Delta E_{\text{B-M}} = \left(\hbar^2/2m_{\text{p}}^*\right)[3\pi^2(p/N_{\text{K}})]^{2/3}$ where m_{p}^* is the effective hole mass, N_{K} is the valence band multiplicity factor at the K point (6), and p is carrier density previously determined by Hall-effect measurements[9], the B-M shift $\Delta E_{\text{B-M}}$ is estimated to be ~19 meV for 0.5% doping of Nb. Although the estimated value is comparable to the observed blueshift, this effect alone cannot explain the observation: the B-M shift expects a blueshift only in the lowest transition (*i.e.*, the A exciton), while we observed simultaneous blueshift in both the A and B exciton energies in spite of an energy separation of nearly 150 meV between them.

Additionally, the existence of dense hole gas distributed in a monolayer thickness cannot be ignored, since it effectively screens the binding energy of excitons, as recently observed in electrostatically gated[10] and theoretically modelled heavily doped monolayer MX_2[11], both showing blueshifts of exciton resonances. Considering that our nominal 2D hole density (~1.2×10^{13} cm^{-2} for 1% Nb-doped MoS_2) exceeds the maximum carrier density (~8×10^{12} cm^{-2}) previously achieved by field-effect gating, plus additional dielectric screening from charged impurity centres, it is reasonable to expect even stronger effects compared to the reported binding energy reduction in Ref. [1]. However, more investigations are needed along with a quantitative evaluation of bandgap renormalization effects, which tends to counteract the reduction of exciton binding energy.

Supplementary References

1. Suzuki, R. *et al.* Valley-dependent spin polarization in bulk MoS_2 with broken inversion symmetry. *Nat. Nanotechnol.* **9,** 611–617 (2014).
2. Togo, A and Tanaka, I. First principles phonon calculations in materials science. *Scr. Mater.* **108,** 1–5 (2015).
3. Shmeliov, A. *et al.* Unusual stacking variations in liquid-phase exfoliated transition metal dichalcogenides. *ACS Nano* **8,** 3690–3699 (2014).
4. Lin, Y.-C. *et al.* Properties of individual dopant atoms in single-layer MoS_2: atomic structure, migration, and enhanced reactivity. *Adv. Mater.* **26,** 2857–2861 (2014).
5. Lee, J.-U. *et al.* Raman signatures of polytypism in molybdenum disulfide. *ACS Nano* **10,** 1948–1953 (2016).
6. Saigal, N. & Ghosh, S. H-point exciton transitions in bulk MoS_2. *Appl. Phys. Lett.* **106,** 182103 (2015).
7. Saigal, N., Sugunakar, V. & Ghosh, S. Exciton binding energy in bulk MoS_2: a reassessment. *Appl. Phys. Lett.* **108,** 132105 (2016).
8. Sun, Q. C. *et al.* Observation of a Burstein–Moss shift in rhenium-doped MoS_2 nanoparticles. *ACS Nano* **7,** 3506–3511 (2013).
9. Suh, J. *et al.* Doping against the native propensity of MoS_2: degenerate hole doping by cation substitution. *Nano Lett.* **14,** 6976–6982 (2014).
10. Chernikov, A. *et al.* Electrical tuning of exciton binding energies in monolayer WS_2. *Phys. Rev. Lett.* **115,** 126802 (2015).
11. Gao, S., Liang, Y., Spataru, C. D. & Yang, L. Dynamical excitonic effects in doped two-dimensional semiconductors. *Nano Lett.* **16,** 5568–5573 (2016).